Statistical fatigue properties and small fatigue crack propagation in bimodal harmonic structured Ti-6Al-4V alloy under four-point bending

Kikuchi, Shoichi ; Kubozono, Hiroki ; Nukui, Yuhei ; Nakai, Yoshikazu ; Ueno, Akira ; Kawabata, Mie Ota ; Ameyama, Kei

(Citation)
Materials Science and Engineering: A,711:29-36

(Issue Date)
2018-01-10

(Resource Type)
journal article

(Version)
Accepted Manuscript

(URL)
https://hdl.handle.net/20.500.14094/90004628

Title page

Statistical Fatigue Properties and Small Fatigue Crack Propagation in Bimodal Harmonic Structured Ti-6Al-4V Alloy under Four-point Bending

Shoichi KIKUCHI [a,*], Hiroki KUBOZONO [a], Yuhei NUKUI [a], Yoshikazu NAKAI [a], Akira UENO [b], Mie Ota KAWABATA [b] and Kei AMEYAMA [b]

[a] Department of Mechanical Engineering, Graduate School of Engineering, Kobe University, 1-1 Rokkodai-cho, Nada-ku, Kobe, 657-8501, JAPAN

[b] Department of Mechanical Engineering, College of Science and Engineering, Ritsumeikan University, 1-1-1 Noji-higashi, Kusatsu, Shiga, 525-8577, JAPAN

*: Corresponding author

E-mail address: kikuchi@mech.kobe-u.ac.jp,

Phone: +81-78-803-6329, Fax: +81-78-803-6155

Abstract

Small fatigue crack propagation in bimodal harmonic structured titanium alloy (Ti-6Al-4V) with high strength and ductility was examined under four-point bending at a stress ratio of 0.1 in the ambient laboratory atmosphere. The crack profiles were observed using optical microscopy and scanning electron microscopy, and analyzed using an electron backscattered diffraction to examine the mechanism of small fatigue crack propagation. Fatigue crack paths were not influenced by the bimodal harmonic structure, and the crack growth rates, da/dN, in the harmonic structured Ti-6Al-4V were almost the same as those in a material with coarse acicular microstructure for comparable values of stress intensity range, ΔK. In contrast, the harmonic structured Ti-6Al-4V had a higher resistance of fatigue crack initiation due to the grain refinement induced by mechanical milling, which resulted in an increase of the fatigue life and fatigue limit. Furthermore, the statistical fatigue properties of Ti-6Al-4V alloy were analyzed using the stress dependence of Weibull parameters to quantitatively examine the effects of the bimodal harmonic structure on its fatigue life.

Keywords

Fatigue; Fracture mechanics; Titanium alloy; Grain refinement; Spark plasma sintering; Statistical analysis

1. Introduction

Titanium alloys have been used in various engineering fields and products, such as aerospace components [1], energy industry applications [2], marine applications [3], biomaterials [4,5], and consumer applications (e.g., watch bands) [6], because titanium alloys exhibit high specific strength, high heat resistance, and excellent corrosion resistance. In recent years, demand has been increasing for improvement in the mechanical properties of titanium alloys, including the Ti-6Al-4V alloy featured in this study, and reduction of the cost of titanium products [7]; therefore, increasing the structural reliability of Ti-6Al-4V alloy has become an important research effort.

The microstructure and mechanical properties of Ti-6Al-4V alloy can be controlled by heat treatment [8,9], the addition of different elements (boron [10,11] and niobium/molybdenum [12]), and grain refinement [13,14]. In particular, grain refinement using severe plastic deformation is an effective approach for strengthening metallic materials based on the Hall-Petch relationship [15,16]. In contrast, to prevent a decrease in ductility of materials [13] due to the formation of homogeneous fine-grained structure, bimodal microstructural designs were proposed [17-19]. Our group also has developed a harmonic structure design using powder metallurgy to sinter mechanically milled Ti-6Al-4V powders [20-22], which improves both their strength and ductility by suppressing necking during tensile deformation [23].

In particular, we have focused on the fatigue properties [22,24] and near-threshold

fatigue propagation of long cracks [25-27], which depend on the stress ratio (the ratio of minimum to maximum stress) [8,28] for Ti-based materials with a bimodal microstructure. However, to achieve sufficient performance for the newly developed materials for practical applications, small fatigue crack propagation needs to be examined due to the differences in the threshold stress intensity range, ΔK_{th}, for small and long cracks [29,30]. Previous studies examined small fatigue crack propagation in conventional Ti-6Al-4V alloys [8,31-36]; Nakajima et al. [31] reported that fatigue cracks were initiated in α grains as stage-I cracks in a conventional Ti-6Al-4V alloy and their propagation direction changed at the grain boundary. Another important aspect in the newly developed materials is an evaluation of fatigue life scatter [37,38], which occurs even if highly controlled techniques for material preparation are employed. The authors previously [37] proposed the approach of evaluating the statistical fatigue properties of Zr-based bulk metallic glass using the distribution of the normalized time strength.

The purpose of this study is to examine small fatigue crack propagation in bimodal harmonic structured Ti-6Al-4V alloy with high strength and ductility under four-point bending. Furthermore, the statistical fatigue properties of this alloy are analyzed to quantitatively examine the effects of the harmonic structure on its fatigue life.

2. Experimental procedure

2.1 Material and microstructural characterization

This study employed Ti-6Al-4V alloy containing 6.51% Al, 4.26% V, 0.17% Fe, 0.0023% H, 0.003% N, 0.18% O, and 0.01% C (all by mass, with the balance being Ti). This material was made into a powder (186-μm particle diameter) using a plasma rotating electrode process, which can be used to fabricate spherical particles that have negligible contamination by impurities such as oxygen or nitrogen gas [39].

Bimodal microstructural design using mechanical milling (MM) and spark plasma sintering (SPS) was introduced for the formation of the harmonic structured Ti-6Al-4V alloy, as defined in later. MM was performed for 90 ks in an Ar gas atmosphere at room temperature for the Ti-6Al-4V powders using a planetary ball mill (Fritch P-5) with a tungsten carbide vessel and steel ball bearings to form fine grains at the particle surfaces. The rotation speed was 200 rpm, and the ball-to-powder mass ratio was 1.8:1. The powders were subsequently consolidated by SPS at 1123 K for 1.8 ks under vacuum (less than 15 Pa) and applied pressure (50 MPa) using a 25-mm internal diameter graphite die to produce the specimens referred to herein as the “MM series.” A second set of specimens was prepared by sintering the as-received powders (referred to herein as the “untreated series”) for comparison. The tensile strength for the MM series (956 MPa) was higher than that for the untreated series (864 MPa), but the elongation for the MM series (22.0%) is slightly higher than that for the untreated series (20.9%) [22].

The microstructure of sintered compacts was characterized using electron backscattered diffraction (EBSD) at an accelerating voltage of 20 kV. The inverse pole figure

(IPF) map obtained by EBSD analysis for the MM series is shown in Fig. 1. The MM series contained regions of fine equiaxed grains and regions with a coarse acicular microstructure. The regions of fine equiaxed grains formed a continuous connected three-dimensional network structure that surrounded the coarse acicular microstructure. This network structure is referred to as a harmonic structure in this study.

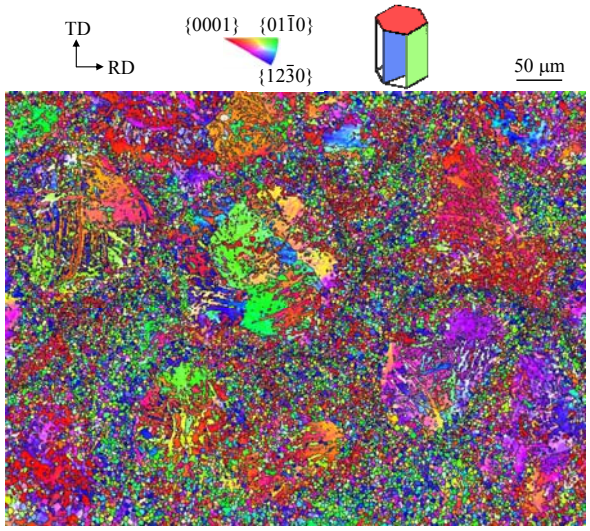

Fig. 1. IPF map obtained by EBSD analysis for MM series with a continuous connected three-dimensional network structure of fine equiaxed grains that surrounded the coarse acicular microstructure.

2.2 Fatigue tests

The sintered materials (10 mm thick, 25 mm diameter) were sliced into disks approximately 1.5 mm thick and machined into a blunt notched specimen with the dimensions shown in Fig. 2. After machining, the specimen surface was polished with emery paper (#240 to #4000) to a thickness of 1 mm and polished in a SiO_2 suspension to obtain a mirror finish. The notch roots of the specimen were also polished with emery paper (#240) to remove the electro-discharge machined layer.

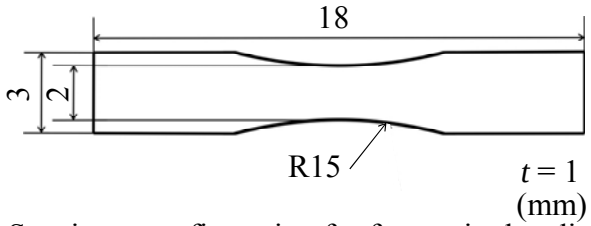

Fig. 2. Specimen configuration for four-point bending fatigue tests.

Four-point bending fatigue tests were performed in an electrodynamic fatigue testing apparatus under a stress ratio R of 0.1. The frequency of stress cycling was 10 Hz, and the tests were conducted in the ambient laboratory atmosphere. Fatigue tests were interrupted at a given number of cycles and acetyl cellulose films were placed on the specimen surface based on the replica method to examine the propagation of fatigue cracks. The stress intensity range, ΔK, was calculated based on the crack length observed by optical microscopy [40], where the aspect ratio, c/a, for small cracks was estimated by the following equations:

$$c/a = 1 - 1.607(a/t) + 1.080(a/t)^2 - 0.2149(a/t)^3 \quad \text{for } a/t < 1 \quad (1)$$

$$c/a = 0.259 \quad \text{for } a/t \geq 1 \quad (2)$$

where a is the crack length in the surface, c is the crack length in thickness directions and t is the thickness of the specimen.

After the fatigue tests, the fracture surfaces and crack profiles were observed using scanning electron microscopy (SEM) and the microstructure around the crack paths was analyzed using EBSD to examine the mechanism of small fatigue crack propagation in the harmonic structured Ti-6Al-4V alloy.

3. Results and discussion

3.1 *S-N* characteristics of harmonic structured Ti-6Al-4V alloy

Fig. 3 shows the results of four-point bending fatigue tests for the sintered compacts (untreated and MM series); a stress amplitude, σ_a, was applied to the specimen surface as a function of the number of cycles to failure, N_f. In this figure, those plots with an arrow represent the run-out specimens without failure at $N = 10^7$ cycles, and each *S-N* curve was determined by adopting the *S-N* model with a fatigue limit in the Japan Society of Materials Science (JSMS) standard regression models [41]. The regression *S-N* curves for both series are expressed by the following formulas:

MM series: $\sigma_a = -125.80\log(N) + 904.64$ (3)

Untreated series: $\sigma_a = -132.70\log(N) + 909.47$ (4)

where σ_a is the stress amplitude (MPa) and N is the number of cycles.

The fatigue limit, σ_w, which was defined based on the JSMS standard [41], was higher for the MM series (280 MPa) than for the untreated series (190 MPa). In addition, the fatigue lives for the MM series were slightly longer than those for the untreated series. However, the knee point, N_w, in the *S-N* curve for the MM series (9.23×10^4) was shorter than N_w for the untreated series (2.50×10^5). We attribute this trend to a large fatigue life scatter for the MM series, where some specimens failed at σ_a = 280 MPa, while one specimen did not

fail at $N = 10^7$ cycles. As a result of observing the fracture surfaces of the MM series, two types of fracture modes were observed: failure at the edge and failure at the mirror-finished surface. Therefore, in Fig. 3, solid symbols represent specimen failure at the edge and open symbols represent specimen failure at the surface. Fig. 3 also reveals that most of the MM series failed at the edge with a shorter fatigue life, whereas only one untreated series compact failed at the edge. This result is attributed to a high notch sensitivity in the MM series due to the high strength.

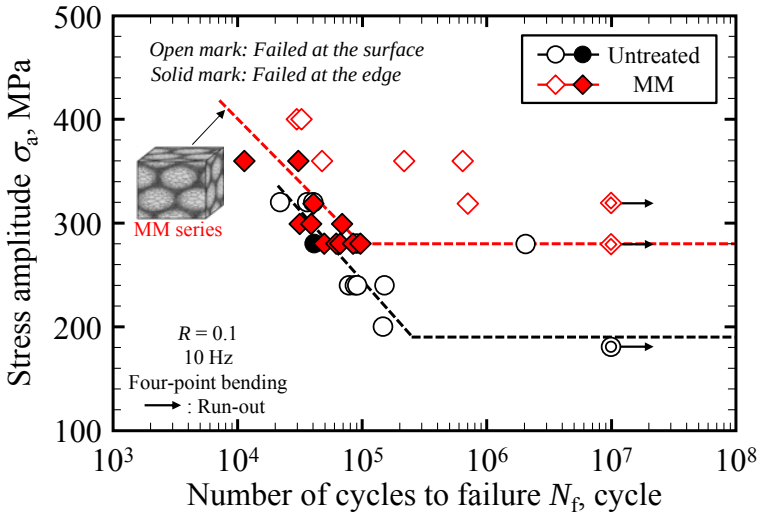

Fig. 3. Results of four-point bending fatigue tests, showing stress amplitude as a function of cycles to failure explaining that MM series has the higher fatigue limit and fatigue life.

To more closely examine the effect of fracture modes on the fatigue properties, the fatigue test data are replotted with each fracture mode presented separately in Fig. 4. The regression *S*-*N* curves for the untreated and MM series for both failure modes are expressed by the following formulas:

MM series, failed at the edge: $\sigma_a = -97.67\log(N) + 758.95$ (5)

MM series, failed at the surface: $\sigma_a = -38.81\log(N) + 564.86$ (6)

Untreated series, failed at the surface: $\sigma_a = -140.62\log(N) + 947.55$ (7)

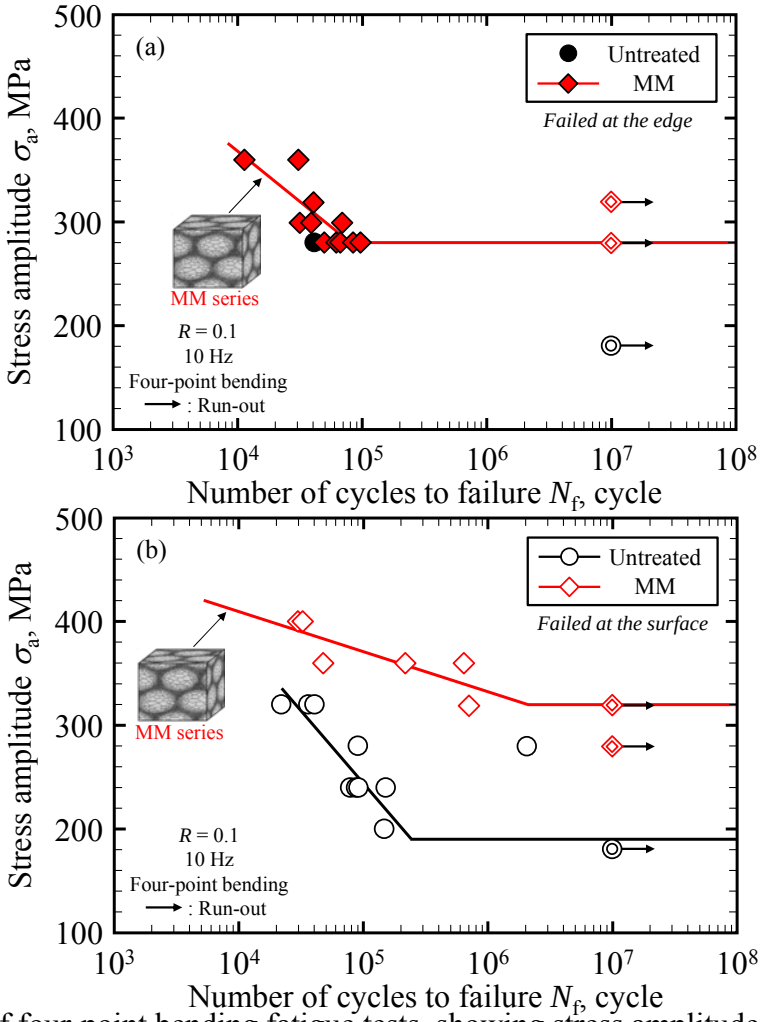

Fig. 4. Results of four-point bending fatigue tests, showing stress amplitude as a function of cycles to failure for specimens that failed at the (a) edge and (b) surface explaining that fractures at the edge decrease the fatigue limit and the fatigue life.

Since the number of fatigue test data points for untreated compacts that failed at the edge was insufficient to obtain an *S-N* curve, *S-N* curve was analyzed only for the data from the MM series in Fig. 4(a).

For the specimens failing at the edge at σ_a = 280 MPa (Fig. 4(a)), the fatigue lives for the MM series were almost the same as those for the untreated series. In contrast, the knee point, N_w, in the *S*-*N* curve analyzed for the MM series failing at the surface (2.04×10^6) was longer than N_w for the untreated series (2.40×10^5), as shown in Fig. 4(b). Furthermore, the fatigue limit, σ_w, and knee point, N_w, in the *S*-*N* curve analyzed for the MM series failing at the surface (320 MPa and 2.04×10^6, respectively) were higher than those of the MM series failing at the edge (280 MPa and 8.01×10^4, respectively). These results imply that fractures at the edge decrease the fatigue limit and the fatigue life of Ti-6Al-4V alloy.

Consequently, the fatigue properties of Ti-6Al-4V alloy with harmonic structure were confirmed to be influenced by two types of fracture modes, but the harmonic structured Ti-6Al-4V alloy exhibited superior four-point bending fatigue properties rather than the material with coarse acicular microstructure (i.e., the untreated series).

3.2 Statistical analysis for the fatigue properties of harmonic structured Ti-6Al-4V alloy

In this section, the effect of the harmonic structure design on the fatigue life distribution of Ti-6Al-4V alloy was examined by applying the three-parameter Weibull distribution concept. In the case of the three-parameter Weibull distribution, the cumulative distribution function, $F(N_f)$, is expressed by the following formula:

$$F(N_f) = 1 - \exp\{-(N_f - \gamma)/\beta)^{\alpha}\}, \qquad (8)$$

where N_f is the number of cycles to failure, α is a shape parameter, β is a scale parameter, and γ is a location parameter. In the case of the original equation based on a two-parameter Weibull distribution concept, γ is equal to 0 because it is not easy to estimate γ. These parameters are obtained by means of the correlation coefficient method proposed by Hoshide et al. [42].

The cumulative failure probability, $F(x_i)$ of the ith datum, x_i, at the ordinate is calculated by the following formula:

$$F(x_i) = i - 0.3/(n + 0.4) \quad (9)$$

where n is the total number of specimens tested at the same stress level.

Weibull plots for both series are shown in Fig. 5, where Fig. 5(a) indicates the fatigue life distribution for the untreated series failing at σ_a = 240 MPa and Fig. 5(b) shows the fatigue life distributions for the MM series failing at σ_a = 280, 300, and 360 MPa. When the number of data points is insufficient to estimate the Weibull parameters, the location parameter is estimated as $\gamma = 0$ [43]; therefore, the distribution characteristics of the fatigue life for every sintered compact are well represented by a three-parameter Weibull distribution in this study. Fig. 5(b) also revealed that the Weibull plots for the MM series varied according to the stress amplitude, σ_a.

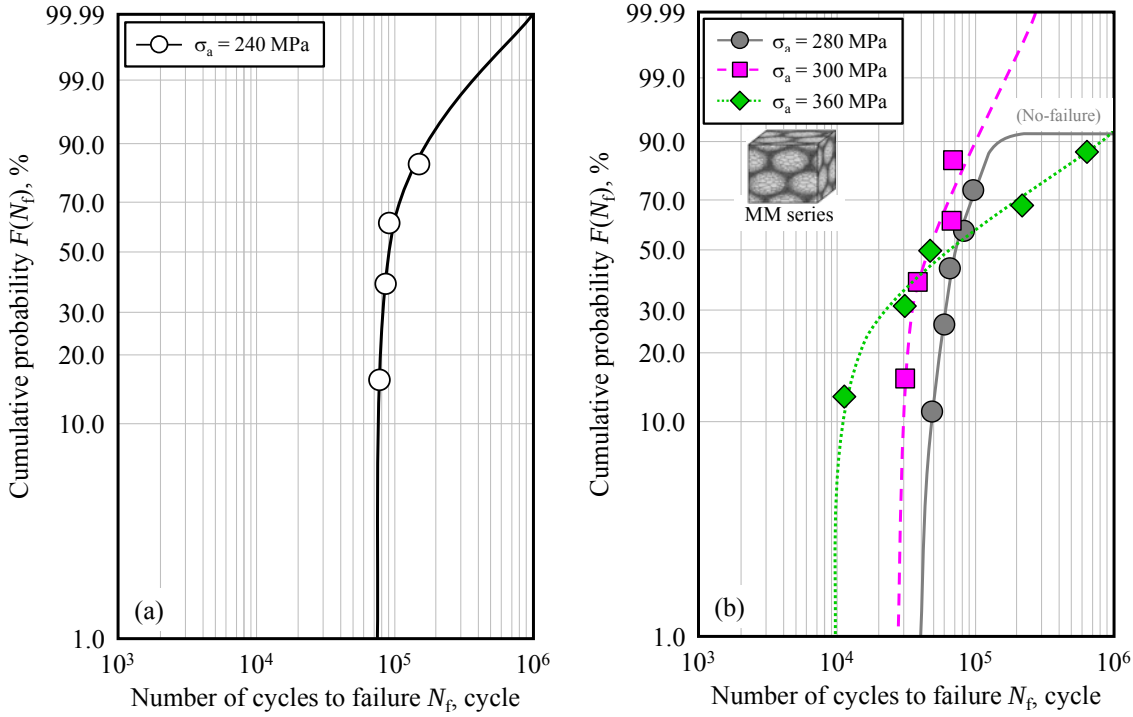

Fig. 5. Weibull plots of fatigue life distributions for (a) untreated series and (b) MM series

explaining that the distribution characteristics of the fatigue life are well represented by a three-parameter Weibull distribution.

Weibull parameters obtained at the respective stress levels are plotted in Fig. 6 as a function of the stress amplitude, σ_a. Fig. 6(a) shows that the shape parameter, α (Weibull modulus), tends to decrease linearly with increasing stress amplitude in the MM series. This result indicates that fatigue life scatter in both fracture modes of the MM series becomes larger with increasing stress amplitude. In Fig. 6(b) for the MM series, the scale parameter, β, tended to increase with increasing stress amplitude, whereas the location parameter, γ, tended to decrease linearly with increasing stress amplitude. Thus, the stress dependence of the Weibull parameters was clearly observed for the harmonic structured Ti-6Al-4V alloy.

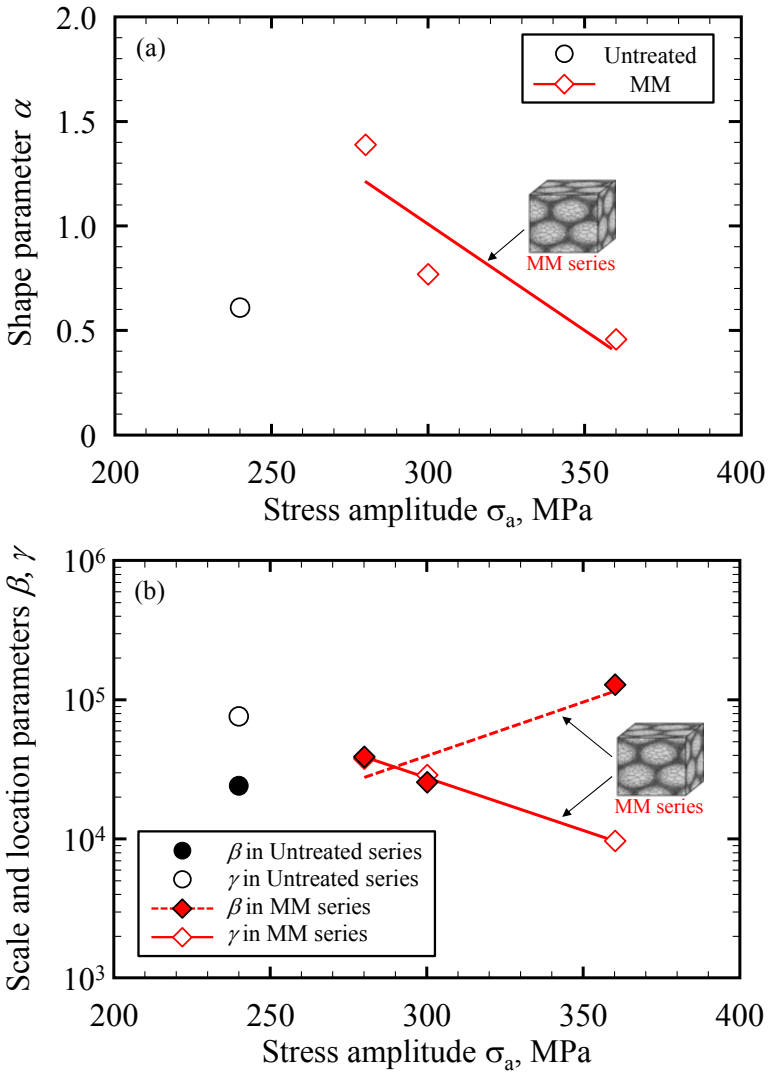

Fig. 6. Dependence of Weibull parameters on stress amplitude for (a) shape parameter and (b) scale and location parameters in an approximately linear correction.

In this study, the location parameter, γ, corresponds to the minimum value of N_f; therefore, γ values obtained at the respective stress levels are plotted in Fig. 7 as a function of the number of cycles. The *S-N* curves obtained from all the experimental data (Fig. 3) are also shown in Fig. 7. In the MM series, γ tended to decrease in an approximately linear correlation with increasing number of cycles; the correlation coefficient was -0.998. Furthermore, the plot for γ is lower than the original *S-N* diagram obtained from all experimental data (Fig. 3). The

S-N diagram indicates a failure probability of F = 50%; therefore, the fatigue life for the harmonic structured Ti-6Al-4V alloy can be estimated conservatively by estimating the location parameter using the Weibull distribution.

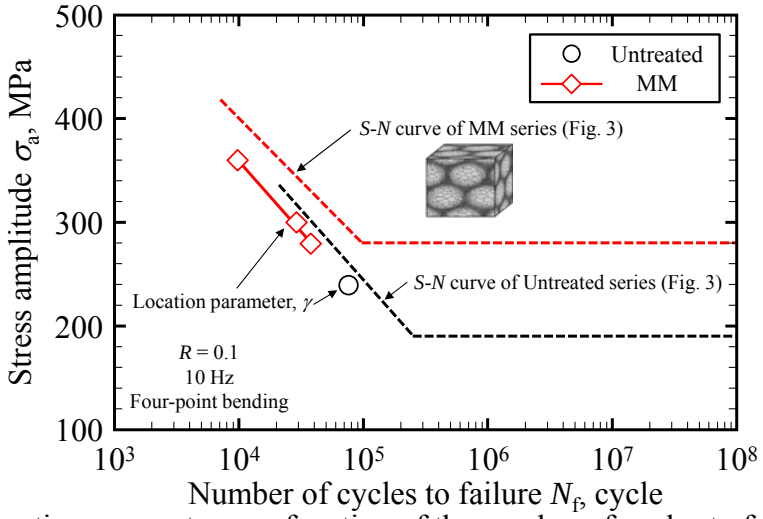

Fig. 7. Location parameter as a function of the number of cycles to failure in an approximately linear correction.

To analyze the *P-S-N* characteristics of the harmonic structure Ti-6Al-4V alloy, a number of fatigue test data are required at the same stress level. However, only one or a few specimens were tested at some other stress levels; therefore, a little rearrangement was conducted on data from both series before performing a statistical analysis of the fatigue characteristics. Fig. 8 presents a schematic illustration of the method for rearranging experimental data for obtaining the fatigue life distribution proposed by Sakai et al. [44]. In this study, a few data points were shifted in parallel with each *S–N* curve obtained from all data for the untreated and MM series, as the life distribution data at the common stress level (300 MPa).

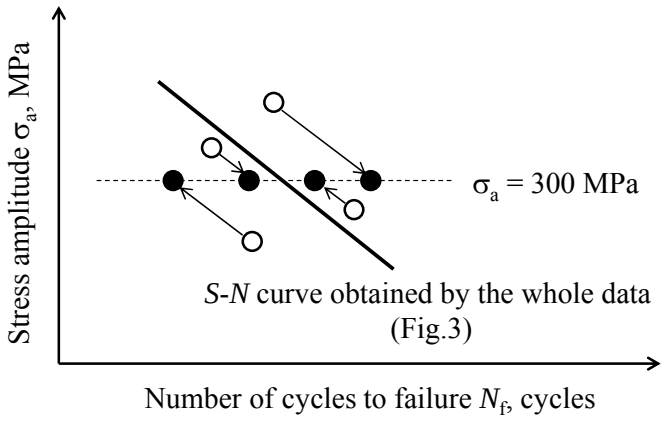

Fig. 8. Schematic explanation of method for rearranging experimental data for obtaining fatigue life distribution data on the basis of Sakai et al. [44].

Fig. 9 shows the Weibull plots of rearranged fatigue life distributions for the Untreated and MM series failed at stress amplitude of 300 MPa. The solid lines in Fig.9 indicate the distribution curves fitted to the rearranged fatigue data and the run-out data are not plotted. The Weibull plots of the MM series were shifted to the longer life than those of the Untreated series. In addition, the location parameter, γ, of the MM series (3.10×10^4) was larger than that of the untreated series (2.65×10^4). These results indicate that a harmonic structure design increases the fatigue life of Ti-6Al-4V alloy.

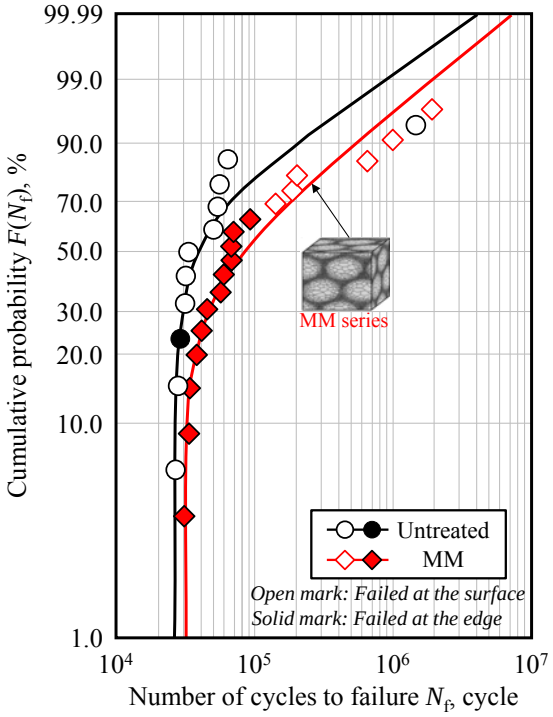

Fig. 9. Weibull plots of rearranged fatigue life distributions for untreated and MM series that failed at stress amplitude of 300 MPa explaining that MM series has the higher fatigue life.

3.3 Small fatigue crack propagation in harmonic structured Ti-6Al-4V alloy

Small fatigue crack propagation was examined based on the replica method to clarify the reason for the increase in the fatigue limit and fatigue life of Ti-6Al-4V alloy caused by the harmonic structure design. Fig. 10 shows optical micrographs of the surface of the MM series tested at σ_a = 360 MPa and observed at given number of cycles. Fig. 10 reveals that no fatigue cracks were observed after 2.00×10^4 cycles (Figs. 10(a) and (b)), but a crack 68 μm long was initiated after 3.00×10^4 cycles (Fig. 10(c)). Subsequently, the crack propagated gradually (Figs. 10(d)-(f)) and the final fracture occurred at 4.72×10^4 cycles. Fig. 11 shows representative features of the fracture surface of the same sample after failure ($N_f = 4.72\times10^4$

cycles). The tensile stress was applied to the upper surfaces shown in the micrograph. A facet-like characteristic microstructure was observed at the surface near the notch root.

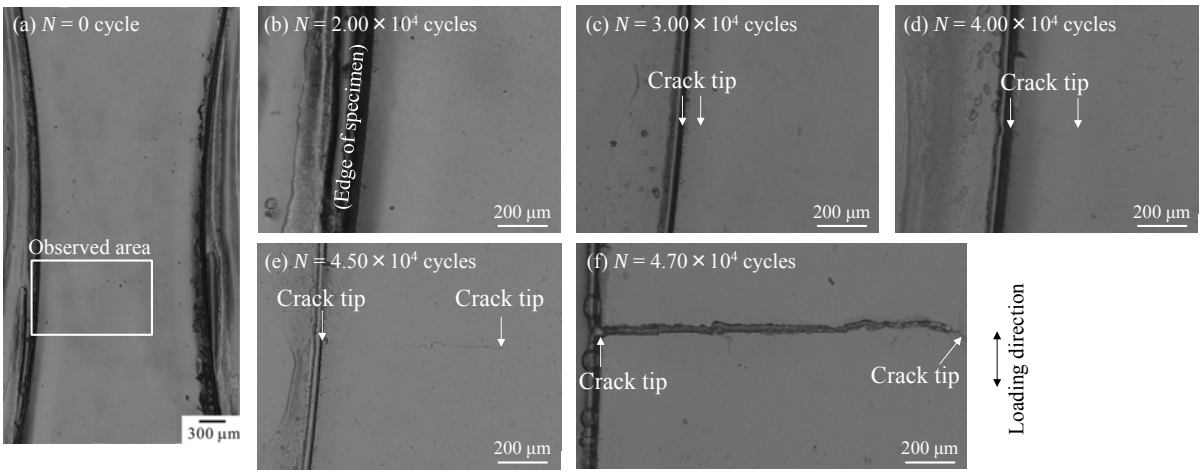

Fig. 10. Optical micrographs of surface of MM series failing at stress amplitude of 360 MPa showing the crack propagation behavior.

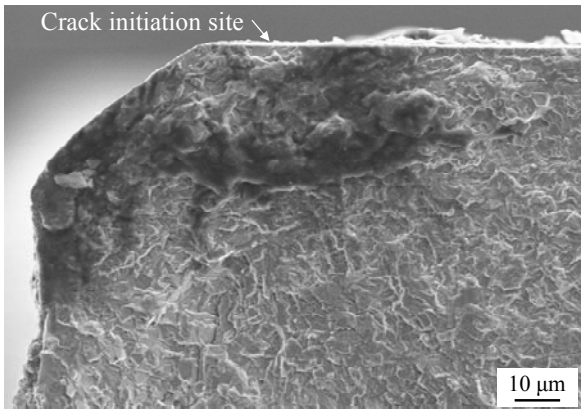

Fig. 11. Representative fracture surface features after failure of sample in Fig. 10 showing the surface fracture mode (σ_a = 360 MPa, $N_f = 4.72 \times 10^4$ cycles).

Fig. 12 presents the dependence of the surface crack length on the number of cycles for the untreated and MM series. A fatigue crack was initiated at $N = 1.00\times10^4$ cycles in the untreated series tested at σ_a = 320 MPa, and increased in length with increasing number of cycles, whereas no cracks were observed in the MM series tested at σ_a = 320 MPa. Cracks were initiated and propagated gradually as the number of cycles increased in the MM series tested at σ_a = 360 and 400 MPa. Furthermore, the crack initiation life of the MM series tended to be short with increased stress amplitude, but it was longer than that for the untreated series tested at σ_a = 320 MPa, although the stress amplitude applied to the MM series was higher. These results indicate that the harmonic structure increases the fatigue crack initiation resistance of Ti-6Al-4V alloy.

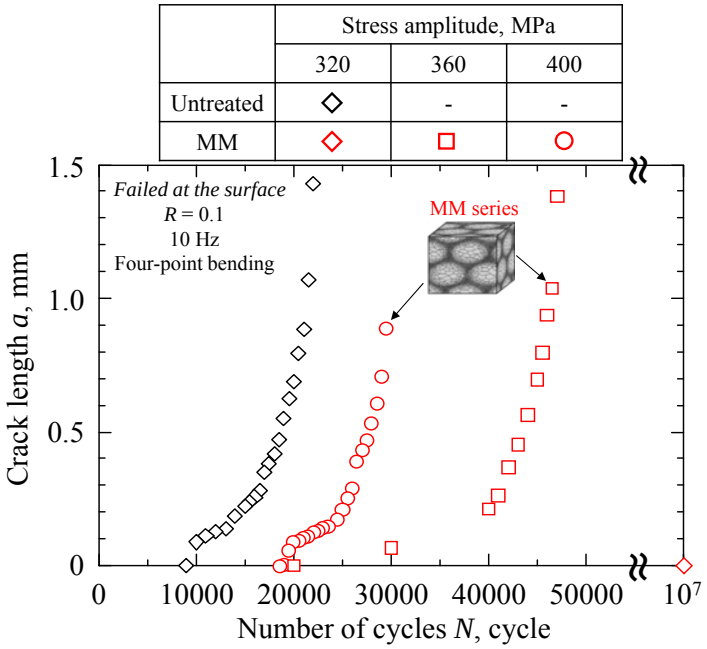

Fig. 12. Crack length as a function of cycles for untreated and MM series explaining that MM series has the higher fatigue crack initiation resistance.

The crack growth rate, da/dN, was calculated using the data shown in Fig. 12. Fig. 13 shows the dependence of the crack growth rate, da/dN, on the stress intensity range, ΔK, for the untreated and MM series. For each series, da/dN increased with increasing ΔK. However, da/dN for the MM series under comparable ΔK was almost the same, regardless of the stress amplitude. Furthermore, there were no noticeable differences in da/dN values between the untreated and MM series at a given applied ΔK. Nalla et al. [8] also reported that the small crack growth rates in a conventional Ti-6Al-4V alloy did not depend on the microstructure, whereas the crack initiation mechanism was influenced by the microstructure.

To discuss the mechanism of the small fatigue crack propagation of Ti-6Al-4V with a bimodal harmonic structure, crack paths were observed and analyzed using EBSD. Fig. 14 presents an IPF map obtained by EBSD near the crack initiation site from the MM series specimen tested at σ_a = 360 MPa. An SEM micrograph of the EBSD analyzed area is also shown in Fig. 14(b). The crack profile for the MM series was smooth regardless of the microstructure, which indicates that the small fatigue crack profile in Ti-6Al-4V alloy is not influenced by the bimodal harmonic structure.

Consequently, a bimodal harmonic structure improves the fatigue properties of Ti-6Al-4V alloy due to an increase of fatigue crack initiation resistance.

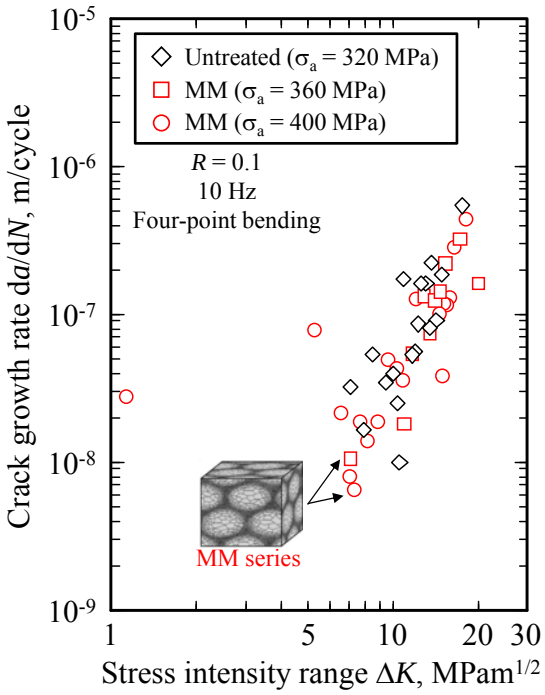

Fig. 13. Relationship between crack growth rate and stress intensity range for untreated and MM series explaining small crack growth rates do not depend on the harmonic structure.

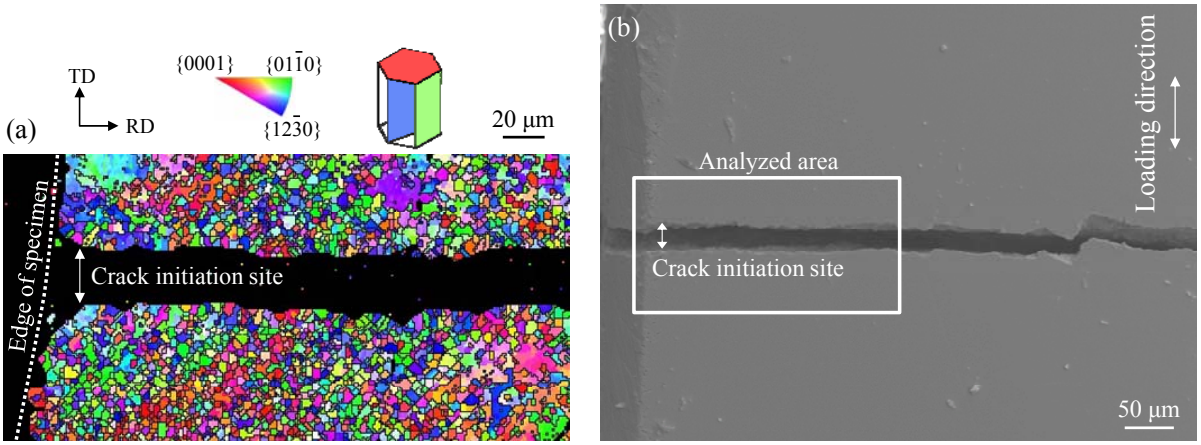

Fig. 14. (a) IPF map obtained by EBSD analysis for MM series specimen that failed at 360 MPa after 4.70×10^4 cycles (N/N_f = 99.6%) and (b) SEM micrograph of the analyzed area explaining that fatigue crack paths are not influenced by the harmonic structure.

3.4 Comparison of small and long crack propagation

Fig. 13 also reveals that a fatigue crack propagated at low ΔK values in the MM series tested at σ_a = 400 MPa, as described in the previous section. In this section, we discuss long crack propagation tests that were also conducted using disk-shaped compact (DC(T)) specimens to compare small fatigue crack propagation with long crack propagation in the bimodal harmonic Ti-6Al-4V alloy.

We conducted *K*-decreasing tests and *K*-increasing tests in ambient air. The test details are published elsewhere [26]. Fig. 15 shows the relationship of the crack growth rates, da/dN, and the stress intensity range, ΔK, for small and long cracks in both series. For small cracks in both series, da/dN values were slightly higher than those for long cracks under comparable ΔK, but the plots were within the same bands. In addition, small cracks in the MM series propagated at ΔK values lower than the threshold stress intensity range, ΔK_{th}, for long cracks (3.2 MPam$^{1/2}$), as shown in Fig. 15(b). The minimum length of crack that we observed in the MM series was 2.4 μm.

For long crack propagation in Ti alloys, the role of crack closure at near-threshold levels is generally attributed to a roughness-induced mechanism [45,46]; therefore, the effective stress intensity range, ΔK_{eff}, was estimated for long cracks in the MM series. The results showed that small cracks in the MM series propagated at ΔK values lower than the effective threshold stress intensity range, $\Delta K_{eff,th}$, for long cracks (3.1 MPam$^{1/2}$). The ΔK_{th} value for small cracks in the MM series is lower than that for long cracks with the elimination

of crack closure.

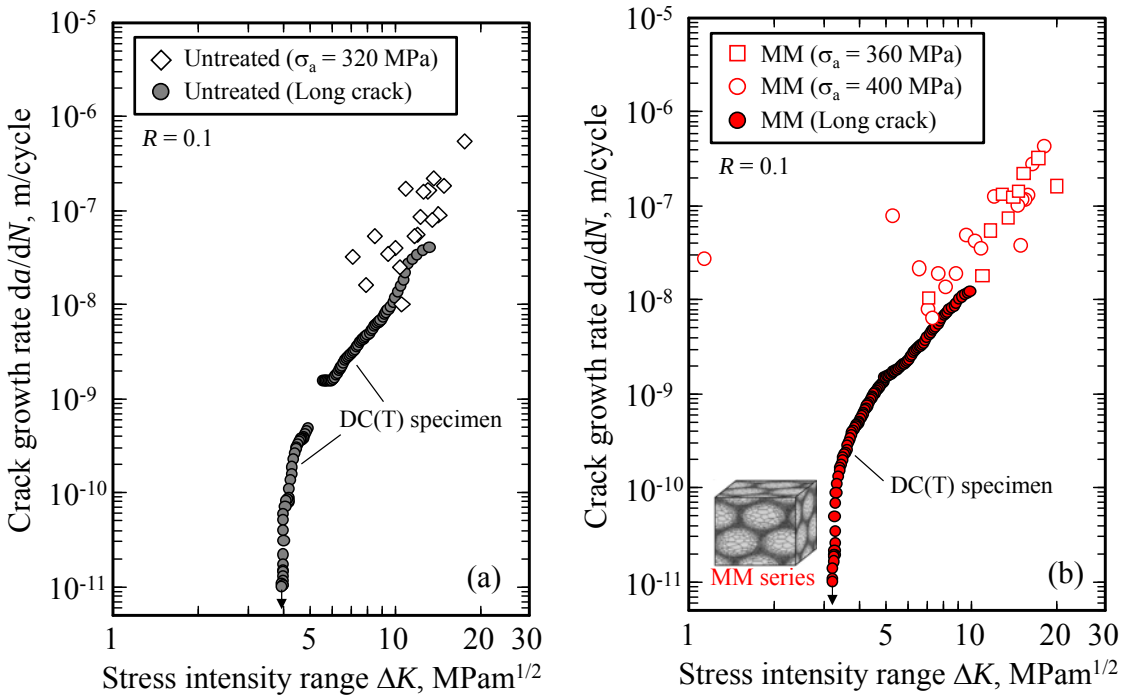

Fig. 15. Relationship between crack growth rate and stress intensity range for (a) untreated series and (b) MM series explaining that small cracks propagate at ΔK values lower than ΔK_{th} for long cracks.

To examine fatigue crack propagation in more detail, the intrinsic crack length, a_0, was estimated by the following formula:

$$a_0 = (\Delta K_{th}/\Delta\sigma_{w0})^2/\pi, \qquad (10)$$

where ΔK_{th} is the threshold stress intensity range for long cracks (MPam$^{1/2}$) and $\Delta\sigma_{w0}$ is the fatigue limit under four-point bending in terms of stress range (MPa).

Fig. 16 shows the relationship between the intrinsic crack length, a_0, and the average grain size calculated by EBSD analysis. The value of a_0 for the MM series was lower than that for the untreated series due to lower ΔK_{th} and higher $\Delta\sigma_{w0}$ than the untreated series. Furthermore, a_0 tended to increase linearly with the average grain size in sintered compacts, which indicates that the grain size has a significant effect on the intrinsic crack length [29]. Thus, the MM series had a shorter path for the propagation of small cracks than the untreated series with the coarse acicular microstructure; therefore, the fatigue crack propagation resistance of the MM series is expected to be slightly higher for crack lengths ranging from $a_{0,MM}$ (10.6 μm) to $a_{0,untreated}$ (34.7 μm), although small fatigue crack growth rates below ΔK_{th} for long cracks could not be obtained in the untreated series.

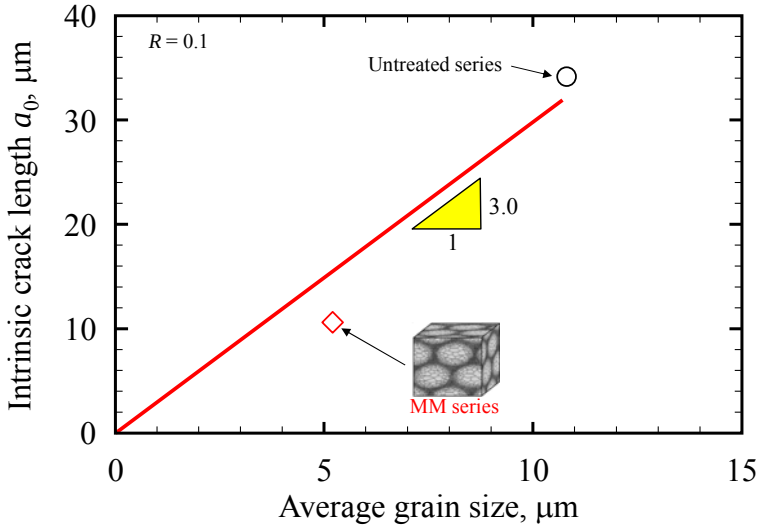

Fig. 16. Intrinsic crack length as function of average grain size in an approximately linear correction.

4. Conclusions

The propagation of small fatigue cracks in a bimodal harmonic structured titanium alloy (Ti-6Al-4V) was examined under four-point bending. Then, the statistical fatigue properties were analyzed using the stress dependence of Weibull parameters to examine the effects of the harmonic structure design on the fatigue life of Ti-6Al-4V alloy. The main conclusions obtained in this study are summarized as follows:

1. The harmonic structured Ti-6Al-4V alloy exhibited a higher fatigue limit and fatigue life than the alloy prepared from as-received powders, which had a coarse acicular microstructure.

2. Based on the stress dependence of the location parameter determined by Weibull analysis of the experimental fatigue data, the statistical fatigue properties of the harmonic structured Ti-6Al-4V alloy can be quantitatively analyzed.

3. Harmonic structure design increases the fatigue crack initiation life for Ti-6Al-4V alloy due to the grain refinement induced by mechanical milling.

4. Small fatigue crack paths are not influenced by the bimodal harmonic structure.

5. The da/dN values in the harmonic structured Ti-6Al-4V alloy are almost the same as those in specimens fabricated from as-received powders for comparable values of stress intensity range, ΔK.

6. The intrinsic crack length in the harmonic structured Ti-6Al-4V alloy was shorter than that in specimens fabricated from as-received powders due to the formation of the fine-grained structure.

Acknowledgement

The authors would like to acknowledge financial support for this work by a JSPS KAKENHI Grant (Number 15K05677) and by The Light Metal Educational Foundation, Inc.

List of references

[1] M. Peters, J. Kumpfert, C.H. Ward, C. Leyens, Titanium alloys for aerospace applications, Adv. Eng. Mater. 5 (2003) 419-427.

[2] R.W. Schuts, H.B. Watkins, Recent developments in titanium alloy application in the energy industry, Mater. Sci. Eng. A 243 (1998) 305-315.

[3] I.V. Gorynin, Titanium alloys for marine application, Mater. Sci. Eng. A 263 (1999) 112-116.

[4] H.J. Rack, J.I. Qazi, Titanium alloys for biomedical applications, Mater. Sci. Eng. C 26 (2006) 1269-1277.

[5] M. Niinomi, Mechanical biocompatibilities of titanium alloys for biomedical applications, J. Mech. Behav. Biomed. Mater. 1 (2008) 30-42.

[6] T. Fujita, A. Ogawa, C. Ouchi, H. Tajima, Microstructure and properties of titanium alloy produced in the newly developed blended elemental powder metallurgy process, Mater. Sci. Eng. A 213 (1996) 148-153.

[7] C. Chunxiang, H. Baomin, Z. Lichen, L. Shuangjin, Titanium alloy production technology, market prospects and industry development, Mater. Design 32 (2011)

1684-1691.

[8] R.K. Nalla, B.L. Boyce, J.P. Campbell, J.O. Peters, R.O. Ritchie, Influence of microstructure on high-cycle fatigue of Ti-6Al-4V: bimodal vs. lamellar structures, Metall. Mater. Trans. A 33 (2002) 899–918.

[9] T. Morita, K. Hatsuoka, T. Iizuka, K. Kawasaki, Strengthening of Ti–6Al–4V alloy by short-time duplex heat treatment, Mater. Trans. 46 (2005) 1681-1686.

[10] I. Sen, S. Tamirisakandala, D.B. Miracle, U. Ramamurty, Microstructural effects on the mechanical behavior of B-modified Ti–6Al–4V alloys, Acta Mater. 55 (2007) 4983-4993.

[11] I. Sen, K. Gopinath, R. Datta, U. Ramamurty, Fatigue in Ti–6Al–4V-B alloys, Acta Mater. 58 (2010) 6799-6809.

[12] A. Kaouka, K. Benarous, A. Daas, S.A. Tsipas, The effects of Nb and Mo addition on microstructure and mechanical behaviour of Ti-6Al-4V alloy, J. of Surf. Sci. Technol. 33 (2017) 53-62.

[13] I.P. Semenova, G.I. Raab, L.R. Saitova, R.Z. Valiev, The effect of equal-channel angular pressing on the structure and mechanical behavior of Ti–6Al–4V alloy, Mater. Sci. Eng. A 387-389 (2004) 805-808.

[14] S. Kikuchi, J. Komotori, Effect of fine particle peening on atmospheric oxidation behavior of Ti-6Al-4V alloy, J. Jpn. Inst. Metals Mater. 80 (2016) 114-120.

[15] E.O. Hall, The deformation and ageing of mild steel: III discussion of results, Proc. Phys. Soc. B 64 (1951) 273–280.

[16] N.J. Petch, The cleavage strength of polycrystals, J. Iron and Steel Inst. 174 (1953) 25–28.

[17] Y. Wang, M. Chen, F. Zhou, E. Ma, High tensile ductility in a nanostructured metal, Nature 419 (2002) 912–915.

[18] J.S. Peter, P.F. David, J. Bertalan, H. Jelena, U. Tamas, Bimodal grain size distribution enhances strength and ductility simultaneously in a low-carbon low-alloy steel, Metallurgical Mater. Trans. A 46 (2015) 1948-1957.

[19] T. Mimoto, J. Umeda, K. Kondoh, Titanium powders via gas-solid direct reaction process and mechanical properties of their extruded materials, Mater. Trans. 56 (2015) 1153-1158.

[20] H. Fujiwara, T. Sekiguchi, K. Ameyama, Mechanical properties of pure titanium and Ti-6Al-4V alloys with a new tailored nano/meso hybrid microstructure, Int. J. Mater. Res. 100 (2009) 796-799.

[21] S.K. Vajpai, M. Ota, T. Watanabe, R. Maeda, T. Sekiguchi, T. Kusaka, K. Ameyama, The development of high performance Ti-6Al-4V alloy by via a unique microstructure design with bimodal grain size distribution, Metall. Mater. Trans. A. 46 (2015) 903–914.

[22] S. Kikuchi, Y. Hayami, T. Ishiguri, B. Guennec, A. Ueno, M. Ota, K. Ameyama, Effect of bimodal grain size distribution on fatigue properties of Ti-6Al-4V alloy with harmonic structure under four-point bending, Mater. Sci. Eng. A 687 (2017) 269-275.

[23] Z. Zhang, D. Orlov, S.K. Vajpai, B. Tong, K. Ameyama, Importance of bimodal

structure topology in the control of mechanical properties of a stainless steel, Adv. Eng. Mater. 17 (2015) 791-795.

[24] S. Kikuchi, K. Takemura, Y. Hayami, A. Ueno, K. Ameyama, Evaluation of the fatigue properties of Ti-6Al-4V alloy with harmonic structure in 4-points bending, J. Soc. Mater. Sci., Jpn. 64 (2015) 880-886.

[25] S. Kikuchi, T. Imai, H. Kubozono, Y. Nakai, A. Ueno, K. Ameyama. Evaluation of near-threshold fatigue crack propagation in Ti-6Al-4V alloy with harmonic structure created by mechanical milling and spark plasma sintering, Frattura ed Integrità Strutturale 34 (2015) 261-270.

[26] S. Kikuchi, T. Imai, H. Kubozono, Y. Nakai, M. Ota, A. Ueno, K. Ameyama, Effect of harmonic structure design with bimodal grain size distribution on near-threshold fatigue crack propagation in Ti-6Al-4V Alloy, Int. J. of Fatigue 92 (2016) 616-622.

[27] S. Kikuchi, T. Mori, H. Kubozono, Y. Nakai, M.O. Kawabata, K. Ameyama, Evaluation of near-threshold fatigue crack propagation in harmonic-structured CP Titanium with a bimodal grain size distribution, Eng. Fract. Mech. 181 (2017) 77-86.

[28] B.L. Boyce, R.O. Ritchie, Effect of load ratio and maximum stress intensity on the fatigue threshold in Ti-6Al-4V, Eng. Fract. Mech. 68 (2001) 129–147.

[29] K. Tanaka, Y. Nakai, M. Yamashita, Fatigue growth threshold of small cracks, Int. J. Fract. 17 (1981) 519-533.

[30] S. Suresh, R.O. Ritchie, Propagation of short fatigue cracks, Int. Metals Rev. 29 (1984)

445–476.

[31] M. Nakajima, K. Terao, T. Miyata, The effect of microstructure on fatigue crack propagation of α+β titanium alloys in-situ observation of short fatigue crack growth, Mater. Sci. Eng. A 243 (1998) 176-181.

[32] F. Cao, K.S.R. Chandran, The role of crack origin size and early stage crack growth on high cycle fatigue of powder metallurgy Ti-6Al-4V alloy, Int. J. Fatigue 102 (2017) 48-58.

[33] F. Yoshinaka, T. Nakamura, S. Nakayama, D. Shiozawa, Y. Nakai, K. Uesugi, Non-destructive observation of internal fatigue crack growth in Ti-6Al-4V by using synchrotron radiation μCT imaging, Int. J. Fatigue 93 (2016) 397-405.

[34] V. Sinha, C. Mercer, W.O. Soboyejo, An investigation of short and long fatigue crack growth behavior of Ti–6Al–4V, Mater. Sci. Eng. A 287 (2000) 30-42.

[35] I. Bantounas, T.C. Lindley, D. Rugg, D. Dye, Effect of microtexture on fatigue cracking in Ti–6Al–4V, Acta Mater. 55 (2007) 5655-5665.

[36] J.H. Zuo, Z.G. Wang, E.H. Han, Effect of microstructure on ultra-high cycle fatigue behavior of Ti–6Al–4V, Mater. Sci. Eng. A 473 (2008) 147-152.

[37] S. Kikuchi, Y.B. Zhang, A. Sakaida, Y. Yokoyama, A. Ueno, T. Sakai, Statistical duplex *S-N* characteristics of bulk amorphous alloy in rotating bending in very high cycle regime, Key Eng. Mater. 664 (2016) 295-304.

[38] W. Li, T. Sakai, M. Wakita, S. Mimura, Influence of microstructure and surface defect on very high cycle fatigue properties of clean spring steel, Mater. Sci. Eng. A 60 (2014)

48-56.

[39] M. Tokizane, K. Isonishi, Production of uniformly-sized spherical powder by plasma rotating electrode process and its applications to some intermetallics powders, J. Jpn. Soc. Powder Metal. 39 (1992) 1137-1144.

[40] J.C. Newman, I.S. Raju, Stress-intensity factor equations for cracks in three-dimensional finite bodies subjected to tension and bending loads, NASA Technical Memorandum 85793, NASA Langley Res. Ctr., Hampton, VA (1984).

[41] T. Sakai (Chair of Editorial Committee) et al., Standard evaluation method of fatigue reliability for metallic materials –standard regression method of S-N curves-, JSMS-SD-11-07, The Society of Materials Science, Japan, (2007).

[42] T. Hoshide, T. Sakai, A. Sakaida, Theory of extremes (part 3), works of Weibull(ii), Sci. Mach. 48 (1996) 1190-1194.

[43] T. Sakai, T. Tanaka, Parameter estimation of Weibull-type-fatigue life distributions including non-failure probability, Proc. 2nd Int. Fatigue Conf. 2 (1984) 1125-1137.

[44] T. Sakai, B. Lian, M. Takeda, K. Shiozawa, N. Oguma, Y. Ochi, M. Nakajima, T. Nakamura, Statistical duplex *S-N* characteristics of high carbon chromium bearing steel in rotating bending in very high cycle regime, Int. J. Fatigue 32 (2010) 497-504.

[45] T. Ogawa, K. Tokaji, K. Ohya, The effect of microstructure and fracture surface roughness on fatigue crack propagation in a Ti-6Al-4V alloy, Fatigue Fract. Eng. Mater. Struct. 16 (1993) 973–982.

[46] K. Sadananda, A.K. Vasudevan, Fatigue crack growth behavior of titanium alloys, Int. J. Fatigue 27 (2005) 1255-1266.

List of figure captions

Fig. 1. IPF map obtained by EBSD analysis for MM series with a continuous connected three-dimensional network structure of fine equiaxed grains that surrounded the coarse acicular microstructure.

Fig. 2. Specimen configuration for four-point bending fatigue tests.

Fig. 3. Results of four-point bending fatigue tests, showing stress amplitude as a function of cycles to failure explaining that MM series has the higher fatigue limit and fatigue life.

Fig. 4. Results of four-point bending fatigue tests, showing stress amplitude as a function of cycles to failure for specimens that failed at the (a) edge and (b) surface explaining that fractures at the edge decrease the fatigue limit and the fatigue life.

Fig. 5. Weibull plots of fatigue life distributions for (a) untreated series and (b) MM series explaining that the distribution characteristics of the fatigue life are well represented by a three-parameter Weibull distribution.

Fig. 6. Dependence of Weibull parameters on stress amplitude for (a) shape parameter and (b) scale and location parameters in an approximately linear correction.

Fig. 7. Location parameter as a function of the number of cycles to failure in an approximately linear correction.

Fig. 8. Schematic explanation of method for rearranging experimental data for obtaining fatigue life distribution data on the basis of Sakai et al. [44].

Fig. 9. Weibull plots of rearranged fatigue life distributions for untreated and MM series that failed at stress amplitude of 300 MPa explaining that MM series has the higher fatigue life.

Fig. 10. Optical micrographs of surface of MM series failing at stress amplitude of 360 MPa showing the crack propagation behavior.

Fig. 11. Representative fracture surface features after failure of sample in Fig. 10 showing the surface fracture mode (σ_a = 360 MPa, $N_f = 4.72 \times 10^4$ cycles).

Fig. 12. Crack length as a function of cycles for untreated and MM series explaining that MM series has the higher fatigue crack initiation resistance.

Fig. 13. Relationship between crack growth rate and stress intensity range for untreated and MM series explaining small crack growth rates do not depend on the harmonic structure.

Fig. 14. (a) IPF map obtained by EBSD analysis for MM series specimen that failed at 360 MPa after 4.70×10^4 cycles (N/N_f = 99.6%) and (b) SEM micrograph of the analyzed area explaining that fatigue crack paths are not influenced by the harmonic structure.

Fig. 15. Relationship between crack growth rate and stress intensity range for (a) untreated series and (b) MM series explaining that small cracks propagate at ΔK values lower than ΔK_{th} for long cracks.

Fig. 16. Intrinsic crack length as function of average grain size in an approximately linear correction.